J. Fluid Mech. (2011), *vol.* 675, *pp.* 268–296.
doi:10.1017/S0022112011000164

The effect of small-amplitude time-dependent changes to the surface morphology of a sphere

A. K. NORMAN[1], E. C. KERRIGAN[2] AND B. J. McKEON[1]†

[1]Graduate Aerospace Laboratories, California Institute of Technology, Pasadena, CA 91125, USA

[2]Department of Aeronautics and Department of Electrical and Electronic Engineering, Imperial College London SW7 2AZ, UK

(Received 23 August 2010; revised 16 December 2010; accepted 23 December 2010; first published online 24 March 2011)

Typical approaches to manipulation of flow separation employ passive means or active techniques such as blowing and suction or plasma acceleration. Here it is demonstrated that the flow can be significantly altered by making small changes to the shape of the surface. A proof of concept experiment is performed using a very simple time-dependent perturbation to the surface of a sphere: a roughness element of 1 % of the sphere diameter is moved azimuthally around a sphere surface upstream of the uncontrolled laminar separation point, with a rotational frequency as large as the vortex shedding frequency. A key finding is that the non-dimensional time to observe a large effect on the lateral force due to the perturbation produced in the sphere boundary layers as the roughness moves along the surface is $\hat{t} = tU_\infty/D \approx 4$. This slow development allows the moving element to produce a tripped boundary layer over an extended region. It is shown that a lateral force can be produced that is as large as the drag. In addition, simultaneous particle image velocimetry and force measurements reveal that a pair of counter-rotating helical vortices are produced in the wake, which have a significant effect on the forces and greatly increase the Reynolds stresses in the wake. The relatively large perturbation to the flow-field produced by the small surface disturbance permits the construction of a phase-averaged, three-dimensional (two-velocity component) wake structure from measurements in the streamwise/radial plane. The vortical structure arising due to the roughness element has implications for flow over a sphere with a nominally smooth surface or distributed roughness. In addition, it is shown that oscillating the roughness element, or shaping its trajectory, can produce a mean lateral force.

Key words: flow control, separated flows

1. Introduction

This research is motivated by the broad goal of understanding the effect of morphing surfaces on wall-bounded flows, with the aim of improving performance and efficiency for a wide range of technologies, as well as utilizing these surfaces to gain insight into the fundamental physical mechanisms that govern the behaviour of the flow. A morphing surface differs from traditional control surfaces such as flaps on an aircraft, in that it may consist of a continuous surface (a 'skin'). The interest is in exciting and utilizing flow instabilities to coerce the flow to perform as desired, with minimal energy input. This is accomplished by making small-amplitude targeted changes to

† Email address for correspondence: mckeon@caltech.edu

the surface morphology, rather than large mechanical changes to the overall shape – a more common use of the term 'morphing'. In this study, we utilize a mechanical approximation to a morphing surface in order to more simply identify the authority of small changes to the surface roughness in influencing the global flow state.

The flow regime of interest in this study was that of the flow over a sphere in which there is a large turbulent wake, with flow separation occurring near the equator (the subcritical regime). For the relatively high Reynolds numbers characteristic of this study, the bluff body flow is characterized by two instabilities, that of the wake and the free shear layer. The spectral distribution of the force acting on a smooth sphere is composed mostly of forces due to vortex shedding and also a lower frequency forcing (Norman & McKeon 2011*b*).

Adding a distributed roughness to the surface causes earlier transition of the boundary layer and leads to a reduced critical Reynolds number, at which the drag coefficient rapidly decreases and reaches a minimum (Achenbach 1974). A single isolated roughness element (a 'stud') produces a side force in the direction of the stud for the subcritical regime, while a force in the opposite direction occurs in the supercritical regime (Norman & McKeon 2011*a*). The wake structure has been described as consisting of counter-rotating vortices with mutual induction away from the sting in the supercritical regime (Taneda 1978) and counter-rotating vortices with mutual induction towards the sting in the subcritical regime (Norman & McKeon 2011*a*).

There have been few studies examining the use of active methods for altering the flow over a sphere. Kim & Durbin (1988) acoustically excited the flow instabilities, leading to an increase in the drag. Jeon *et al.* (2004) were able to achieve a drag reduction at a subcritical Re of 10^5 (where $Re = \rho U_\infty D/\mu$ is based on the sphere diameter D, free stream velocity U_∞, density ρ and dynamic viscosity μ) by applying periodic blowing and suction just upstream of the separation point, thereby producing a similar effect to dimples. They attributed this to exciting the boundary layer instability, which lead to a delayed separation and a laminar separation bubble (similar to the supercritical state).

Though the geometry of the body plays an important role in the specific dynamics of the separation, the fundamental mechanism is the same in many flows: fluid entrainment keeps a flow attached that would otherwise separate. In the context of an airfoil at a high angle of attack, Seifert, Greenblatt & Wygnanski (2004) noted that in order to keep the flow attached using periodic excitation, between one and four vortices from the actuator must be over the body at all times. Darabi & Wygnanski (2004*a*,*b*) have described the temporal evolution of the attachment process, showing that when periodic excitation is abruptly started, the peak lift can be obtained within a dimensionless time of about $\hat{t} \equiv tU_\infty/D = 16$ (where D is the characteristic length, in this case the chord). They also examined the separation process, finding that when the forcing is abruptly stopped, the flow becomes fully detached after about $\hat{t} = 20$.

Using plasma actuation on a circular cylinder, Jukes & Choi (2009*a*, *b*) examined the effect of a single short pulse near the subcritical separation point, finding that the flow was modified for up to $\hat{t} = 40$ after the pulse. Flow visualization revealed that the pulse produced a spanwise vortex, which travelled downstream and momentarily changed the separation point to about 120°. Similarly, Williams *et al.* (2009) examined the effect of a single blowing/suction pulse near the leading edge of a low Reynolds number stalled airfoil, finding that after the disturbance is introduced into the flow, the lift gradually increases until it reaches a maximum after $\hat{t} \approx 3$, and then the lift decays in a similar amount of time.

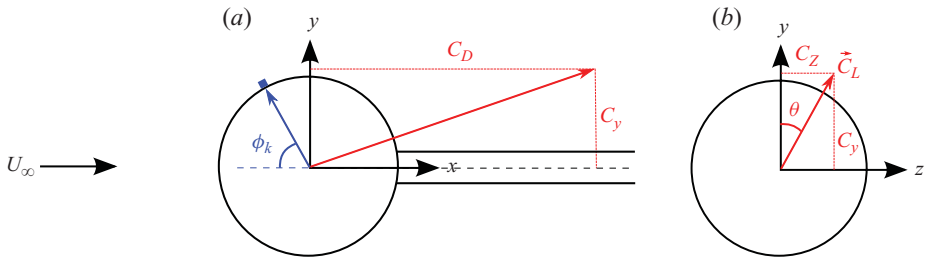

FIGURE 1. (Colour online available at journals.cambridge.org) (*a*) Coordinate system chosen with x as the streamwise direction. The streamwise angle from the stagnation point is ϕ, with the k subscript indicating the streamwise angle to the roughness element. The drag coefficient is C_D. (*b*) Looking downstream: the lateral force coefficient vector is labelled $\vec{C}_L$ and is composed of $C_y\hat{y} + C_z\hat{z}$. The lateral angle from the y-axis to $\vec{C}_L$ is θ. Note that all forces are time-dependent.

This study provides a first step towards understanding the effect of a dynamic surface on the flow field and forces and paves the way for future studies which will utilize true morphing surfaces. Here, a single perturbation to the base geometry is prescribed as a function of time and space, as a simplification of a fully dynamic morphing surface where perturbations are prescribed as a function of time for the entire surface. It is demonstrated that the new experimental apparatus is an excellent testbed for examining the effectiveness of morphing surfaces. In addition, the results of this study give insight into the flow over a sphere with a nominally smooth surface or distributed roughness.

2. Experimental set-up

As true morphing surfaces with a quick response time were not readily available, an experimental apparatus was developed which mimics some of the desired features. In order to demonstrate the potential of a morphing surface, a sphere was chosen as the base geometry, because it is well known that the flow is extremely sensitive to small changes in the surface condition. Small amplitude changes to the surface were produced by moving a small isolated roughness element along the sphere surface at a fixed streamwise angle. Because the flow is so sensitive to the surface finish, the stud was held in place by a small magnet located inside the hollow sphere, which was moved with the use of a small motor, removing the need for slots or other discontinuities in the sphere surface. The forces on a smooth sphere and the effect of a static stud were previously examined in detail (Norman & McKeon 2011*a*, *b*).

The experiments were conducted in a temperature controlled recirculating wind tunnel with a 61 cm × 61 cm × 244 cm test section, which had a free stream turbulence intensity of $\sqrt{\overline{u'^2}}/U_\infty < 0.3\,\%$, where $u'(t) = u(t) - \overline{u}$ is the streamwise fluctuating velocity and $\overline{u}$ is the mean velocity at a point. The mean and unsteady forces were measured using an internal three-component piezoelectric force sensor, and a planar cut of the velocity field was simultaneously obtained using particle image velocimetry (PIV).

The sphere model, shown in figure 2(*a*), was fabricated using selective laser sintering with the DuraForm HST plastic, after which it was finished and a Teflon coating was applied. The sphere had a diameter of 15 cm and consisted of two hollow pieces with a smooth seam located at $\phi = 125°$. The Reynolds number range for this study was $0.5 \times 10^5 < Re < 5.0 \times 10^5$, and the coordinate system is shown in figure 1.

2.1. *Diagnostics*

The sphere was attached directly to a three-component piezoelectric force sensor (Kistler Type 9317B), with dimensions 2.5 cm × 2.5 cm × 3.0 cm. Each of the three piezoelements was connected to a charge amplifier (Kistler 5010B), which output a voltage to a data acquisition board (National Instruments PCI-6014 with a board-2120 connector block). The charge drift associated with piezoelectric sensors was corrected as described in Norman & McKeon (2011 *b*).

The PIV data was taken with simultaneous force measurements by triggering the PIV system using a TTL signal from Labview (which was utilized to collect force data). Image pairs were recorded at 500 Hz for 4 s using a LaVision system consisting of a pulsed ND-YLF laser, a high speed camera with a 1-megapixel CCD (of which only half was used) and 12 bit depth and a computer with a precision timing unit. The phase-averaged results discussed later are based on at least 12 stud revolutions. The laser sheet illuminated an aerosol of bis (2-ethylhexyl) sebacate particles, which have been found to have a mean diameter of 1 μm (Raffel *et al.* 2007), and thus, for the present application, are sufficiently small to accurately follow the flow.

A hot-film was used to examine the state of the boundary layer just upstream of the separation point. The glue-on type sensor (Dantec Dynamics 55R47) was temporarily placed at $\phi_k = 70^\circ$ using a silicone adhesive. The sensing element was a 0.1 mm by 0.9 mm thin nickel layer deposited onto a 50 μm thick Kapton foil base. This caused the sensor to protrude part-way into the boundary layer, which was estimated to have a momentum thickness of less than 100 μm for all operating conditions. Thus, the recorded voltage is related to the shear stress and free stream velocity. The sensor was operated in constant temperature mode using an AA Lab Systems (AN-1005) unit, with an overheat ratio of 1.43, corresponding to a sensor temperature of about 150 °C. For our experiments, a calibration relating the voltage to the shear stress was not necessary (and would have been difficult given that the probe was not flush with the wall) because our primary interests were determining whether the boundary layer was turbulent (based on the intensity of the fluctuations) and understanding the time scales associated with a change to the base flow.

2.2. *Surface actuation*

Surface actuation was achieved with a hollow-core DC motor (MicroMo part number e_2232 − 012SR). This motor was chosen because it was small enough to fit inside the sphere (22 mm in diameter and 41 mm long, including the shaft), and the hollow-core allowed rapid acceleration, as compared to solid-core motors. The arm, attached to the motor shaft (figure 2*b*), was fitted with a magnet at the end of it, positioned approximately 3 mm from the outside surface of the sphere, where a smaller cylindrical magnet was placed (henceforth the 'stud'). The stud had a width and height k such that $k/D = 0.01$ and is shown in figure 3. More details about the selection of this geometry can be found in Norman & McKeon (2011*a*). In what follows, we describe a moving roughness element as a 'dynamic' stud and a stationary element as 'static'. We also consider some results from the smooth sphere for comparison.

As the motor shaft turned, it pulled the stud along the azimuthal direction. The position of the stud was determined from a magnetic encoder attached to the motor, which produced 512 square wave pulses per revolution in two channels (to indicate the direction of rotation). A high-speed camera revealed that the stud followed the desired trajectory to within about $\pm 2^\circ$. The streamwise angle of the stud was chosen to be $\phi_k = 60^\circ$, because a static stud produces the largest force close to this angle (Norman & McKeon 2011*a*).

(*a*) (*b*)

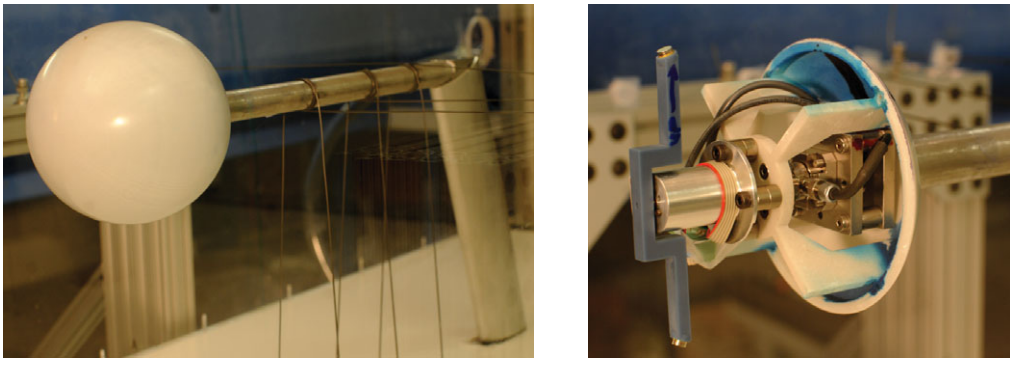

FIGURE 2. (Colour online) (*a*) Model in 61 cm by 61cm recirculating wind tunnel test section, with piano wires used to increase the natural frequency of the sphere-support system. (*b*) Inside of the sphere showing the motor, motor-arm and magnet, and three-component force sensor attached to a stainless steel base.

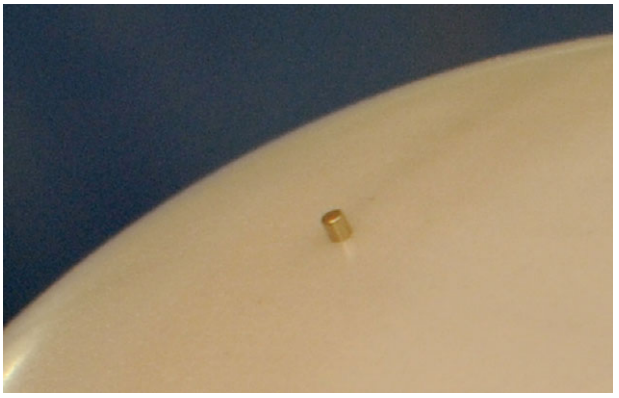

FIGURE 3. (Colour online) Stud with a width and height of $k/D = 0.01$, held in place with a magnet inside the sphere.

The motor was powered by two DC power supplies. The required voltage was calculated in Labview (based on the desired trajectory) and output as a low current voltage signal, which was amplified using an op amp (741) in a power boosting configuration.

In order to reduce the friction between the dynamic stud and the sphere surface, a Teflon pad with a diameter of about $0.03D$ was glued onto the bottom of the stud. The resultant reduced friction between the stud and sphere, combined with the strong neodymium magnets, allowed the stud to move at up to 7 Hz (over $3\,\mathrm{m\,s^{-1}}$), after which point the magnetic pull was not strong enough to keep it attached to the sphere.

In order to eliminate the effect of frictional forces on the force sensor, the motor was attached directly to the sphere instead of the support structure. Thus, the friction force was cancelled by the equal and opposite force on the motor arm. With this configuration the motor had to be precisely balanced (due to centripetal force), a task which was accomplished by making a symmetric arm and attaching small weights until the no-flow lateral forces were negligible at the highest rotation rate.

As will be shown in what follows, an important parameter for manipulating the flow is the relative speed of the stud compared with the flow. Thus, given the experimental constraints, it is beneficial to run at low Reynolds numbers. However, as the Reynolds number is decreased, the forces also decrease, making $Re = 5.0 \times 10^4$ the practical lower limit for our set-up.

2.3. *Actuator controller*

In order to obtain precise control of the motor, which dictates the position of the roughness element, a linear quadratic regulator (LQR) was implemented. Given the importance of the roughness element location and motion to the dynamic actuation studies, and in particular to the shaped trajectories described later, details of the design of the LQR controller with preview control are given in the Appendix. The focus is on controlling the position, but a similar approach was also followed to obtain a separate velocity controller.

The motor dynamics are given by

$$J\ddot{\theta} = K_t i - b\dot{\theta}, \tag{2.1}$$

where θ is the rotational angle, J is the moment of inertia, K_t is the torque constant, i is the current and b is the damping constant. This equation is coupled to the applied voltage by

$$V = L\frac{\mathrm{d}i}{\mathrm{d}t} + Ri + K_t\dot{\theta}, \tag{2.2}$$

where L is the motor inductance, $\varepsilon = K_t\dot{\theta}$ is the electromotive force, $R = R_m + R_s$ is the combination of the motor resistance (R_m) and a small resistor placed in series (R_s), which was used to measure the current.

The physical constants for the motor, as supplied in the specifications, are $J = 2.42 \times 10^{-5}\ \mathrm{N\,m\,s^2}$ (this includes the encoder and the calculated moment of inertia of the rapid-prototyped arm and magnets), $K_t = 1.6 \times 10^{-2}\ \mathrm{N\,m\,A^{-1}}$, $R_m = 4.09\ \Omega$ and $L = 1.80 \times 10^{-4}\ \mathrm{H}$. The damping constant was estimated using the no-load current and no-load speed, giving $b \approx K I_0 \omega_0 = 3.8 \times 10^{-7}\ \mathrm{N\,m\,s}$.

Sampling at 1000 Hz and utilizing the preview controller along with a Kalman filter, excellent trajectory control was obtained, and a similar controller provided precise velocity control. The measured system response agreed well with a Matlab simulation of the motor and controller.

2.4. *Data processing*

In an ideal motor, all of the electrical energy is converted to rotational energy. Neglecting damping, the torque is proportional to the current (2.1). This torque is generated through the Lorentz force F: electrons move through the motor coils, which are surrounded by a magnetic field such that $\boldsymbol{F} = q(\boldsymbol{E} + \boldsymbol{v} \times \boldsymbol{B})$ produces torque. Here q and v are the electron charge and velocity, and E and B are the electric and magnetic fields, respectively. This cross product is very unlikely to produce only a torque, but also a mean force on the motor coils. In most situations this is not a problem because (i) it is only relevant during acceleration, and (ii) most of the energy is converted into torque. Because our motor is located directly on top of the force sensor, this force is detected, interfering with the desired measurement of the forces caused by the flow. However, because the force is directly proportional to the current, a simple correction method can be devised. Since the applied current is measured, the force on the fluid can be recovered as follows: $F_{fluid} = F_{total} - F_{motor}$. The experimentally

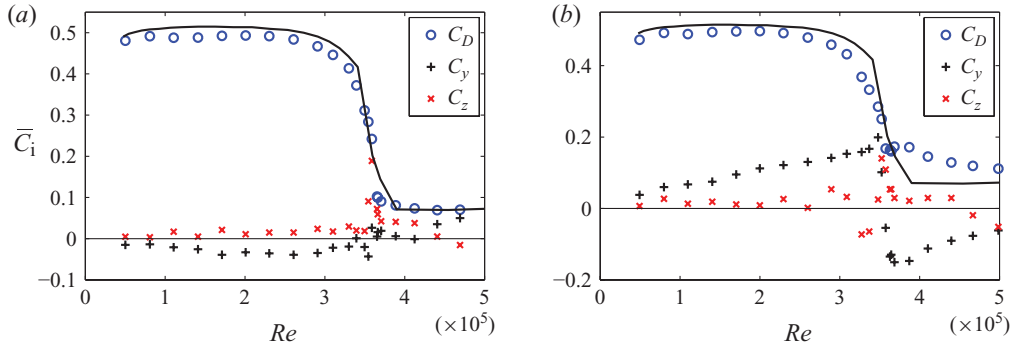

FIGURE 4. (Colour online) Static forces and a comparison with the smooth (−) sphere results from Achenbach (1974): (*a*) smooth sphere results, and (*b*) the same sphere with a $0.01D$ stud placed at $\phi_k = 60°$.

determined correction factor is given by

$$F_{motor} = i(0.088\hat{x} - 0.0625\hat{y} - 0.0145\hat{z}). \tag{2.3}$$

Comparing with the measured torque, this expression indicates a linear mean force of about 6 % of the total force, while 94 % is converted into torque. Note that this equation depends on the motor orientation. With this correction, fairly large oscillating currents only increased the sensor noise by a few millinewtons. The correction was applied to the raw data, before implementing filtering. Note that the large forces attributed in this paper to the interaction of the flow with the stud are not present when there is no flow.

In order to quantify the influence of the dynamic stud on the flow field, the induced forces were examined in a stud reference frame such that the $+y$-direction always pointed towards the stud. This allowed the measurement of the phase even when the unsteady force vector passed through 360°. A coordinate transformation was used on the temporal lateral force data such that the new coordinate system rotated with the stud. Then, the mean C_y and C_z (in the stud frame, based on many rotations) were found and converted to the mean C_L and θ. The data was subsequently processed as in Norman & McKeon (2011 *b*).

Further details about the experimental set-up and data processing can be found in Norman & McKeon (2011*a*, *b*). In what follows, we present results for constant stud rotation speeds and shaped stud trajectories, beginning with the analysis of the flow-induced forces before discussing the changes to the flow field structure.

3. Results: constant speed of stud motion

The forces on the Teflon-coated sphere and the effect of a static stud as a function of Reynolds number are shown in figure 4. The variation of the coefficient of drag is almost identical to the smooth sphere results of Achenbach (1974), and the mean lateral forces in the subcritical regime are near zero, demonstrating that the base sphere model is effectively smooth and allowing the subsequent isolation of the effect produced by a dynamic roughness element. The results are also similar to those for the sphere used by Norman & McKeon (2011*a*), though the critical Reynolds number in this study is higher (indicating that the effective roughness is lower).

Figure 5 shows a time trace of the lateral forces (a lateral force phase plot) for a total time of $\hat{t} = 100$ without a stud and with a dynamic stud moving at two different

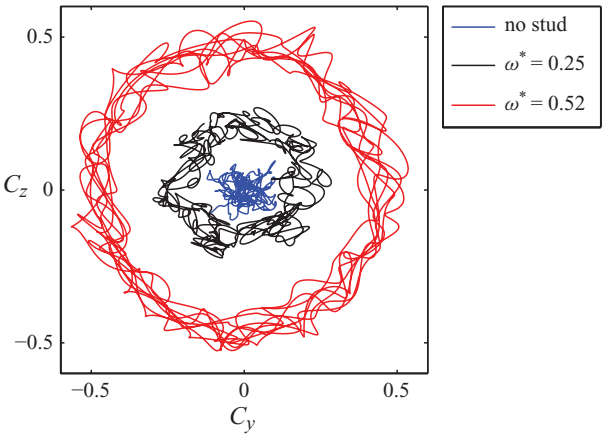

FIGURE 5. Time trace of the lateral force coefficients for $Re = 5 \times 10^4$, showing that the dynamic stud completely changes the force characteristics. The mean of the lateral force magnitude of the moving stud is up to seven times larger than that of the static stud.

constant angular frequencies, expressed as a dimensionless quantity related to the product of stud angular frequency and free stream time scale,

$$\omega^* \equiv \dot{\theta}_k D / U_\infty. \tag{3.1}$$

The phase plot for a static stud (not shown) is very similar to the no stud case, except with a small mean offset (Norman & McKeon 2011*a*). By adding time-dependence to the stud's position, the lateral forces are completely altered with most of the spectral energy centred on the frequency of the stud rotation. Though the net mean force is not altered, the fluctuating forces increase substantially. At any given instant, the magnitude of the (rotating) lateral force is approximately $|\vec{C}_L(\hat{t})| = 0.46$ for $\omega^* = 0.52$, an order of magnitude larger than the mean lateral force due to a static stud. This is surprisingly large considering that the effect is caused by a very small perturbation to the sphere morphology; yet when an entire golf ball spins about an axis perpendicular to its direction of motion at $\dot{\phi} D / U_\infty = 0.52$, it has a mean lateral force coefficient of about 0.2 (Bearman & Harvey 1976) due to the Magnus effect. Not apparent in figure 5 is that the angle to the lateral force vector (θ) lags behind the stud angle, where the phase difference $\theta - \theta_k$ is dependent on the angular frequency.

3.1. *Effect of Reynolds number*

The mean phase difference between the direction of the lateral force and the azimuthal location of the stud is plotted along with the mean of the lateral force magnitude in figure 6 for a large range of Reynolds numbers, showing that ω^* provides very good collapse of the data for subcritical Reynolds numbers. These calculations are based on the mean force in the stud reference frame and were described in § 2.4.

As the stud speed is increased, the lateral force first increases from its static zero-speed value until it reaches a maximum near $\omega^* = 0.5$, after which point it begins to gradually decrease. Note that the magnitude of the lateral force is dependent on the magnitude of the static stud force ($\omega^* = 0$). The stud makes one revolution during an average vortex shedding cycle when $\omega^* = 1.1$. Near this angular frequency there is no amplification of the lateral forces (compared with adjacent frequencies), as might be expected in the case of a resonance with the wake instability, identified by Chomaz,

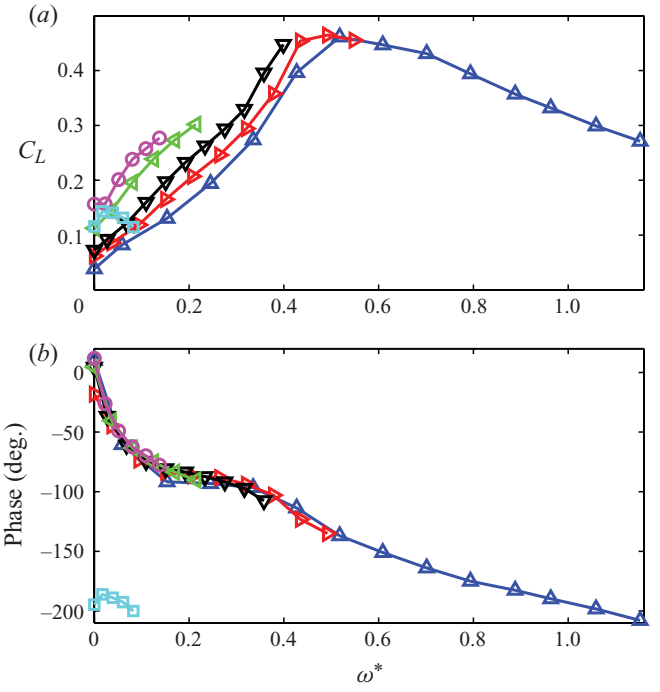

FIGURE 6. (Colour online) (*a*) Mean C_L and (*b*) phase $(\theta - \theta_k)$ (in stud reference frame) vs. dimensionless angular frequency for $Re = 0.5 \times 10^5$ (△); $Re = 0.8 \times 10^5$ (▷); $Re = 1.1 \times 10^5$ (▽); $Re = 2.0 \times 10^5$ (◁); $Re = 3.1 \times 10^5$ (○) and $Re = 4.1 \times 10^5$ (□). All are in the subcritical Re regime except the final one listed is in the supercritical regime.

Bonneton & Hopfinger (2006) as a helical mode instability. However, the peak C_L does occur close to a subharmonic, so a connection cannot be ruled out.

The phase difference between the force vector and stud position exhibits three distinct regimes (figure 6*b*). Firstly, there is a sudden decrease in the phase with increasing ω^*. This levels off near $\theta - \theta_k = -90°$, and then the phase difference begins to decrease nearly linearly beyond $\omega^* = 0.35$. These results are essentially independent of the Reynolds number in the subcritical regime and are not dependent on the magnitude of the static stud force.

The effect of the dynamic stud is quite different in the supercritical regime, as is to be expected because the flow separates turbulently, further downstream. Figure 6 shows a limited range of results for $Re = 4.1 \times 10^5$, indicating that in the supercritical regime the mean lateral force and phase difference do not change significantly over the range of angular frequencies examined. Note also that the phase difference is approximately $-180°$. This is the same phase difference observed for a static supercritical stud (figure 4).

The focus of this paper will be on $Re = 5 \times 10^4$ because the stud has the highest dimensionless speed at this condition. However, figure 6 reveals that the physics appear to be essentially the same over the entire subcritical Reynolds number regime examined here, at least from $5 \times 10^4 < Re < 3.1 \times 10^5$. Thus, the results presented below are applicable to this subcritical range, and more generally, it may be possible to draw conclusions for other bodies that have a variable laminar separation line.

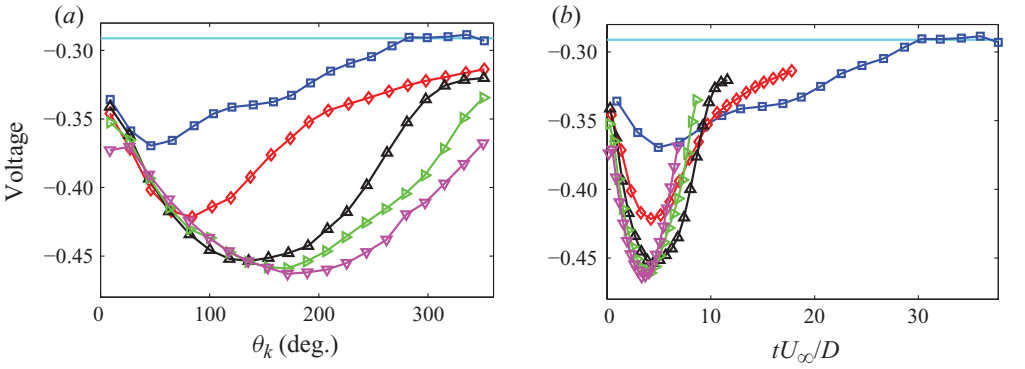

FIGURE 7. (Colour online) (*a*) Uncalibrated hot-film voltage: lower voltage indicates greater heat transfer. Results are for $Re = 5 \times 10^4$ and are averaged over 100 revolutions, as a function of the stud angle, in order to suppress voltage oscillations caused by vortex shedding. (*b*) Normalized with respect to time since the stud passed. No stud mean (—); $\omega^* = 0.15$ (□); 0.34 (◇); 0.52 (△); 0.70 (▷); 0.89 (▽).

3.2. *Flow response time*

Hot-film measurements at $\phi = 70°$ reveal the phase relationship between the azimuthal location of the stud (θ_k) and the local response of the boundary layer at the hot-film location $\theta = 0°$ (figure 7). The vertical axis shows the uncalibrated voltage signal, with a lower voltage indicating greater heat transfer and thus higher velocity/shear stress. The horizontal line shows the mean voltage produced in the absence of a stud, while the other data represent the phase-averaged voltage over many stud revolutions as a function of the stud position with varying angular frequencies. The boundary layer and free shear layer are receptive to disturbances, and it is likely that the passing stud locally triggers these instabilities, which then grow and convect downstream, gradually entraining more fluid and delaying the separation, which would change the velocity near the hot-film. At the lowest frequency, it is seen that the local velocity has time to readjust to the smooth sphere value before the stud makes a full revolution. However, with all of the other speeds the flow does not have time to fully readjust.

In figure 7(*b*) the x-axis was rescaled to show the non-dimensional time since the stud passed instead of the position of the stud, revealing that the flow does not fully respond until $\hat{t} \approx 4$ after the stud has passed. This is similar to the response time of a stalled airfoil to a perturbation of the boundary layer upstream of separation (Williams *et al.* 2009). As will be seen in the flow visualization results presented in the next sections, this time delay is associated with a large-scale change in both the location of flow separation and the wake characteristics.

3.3. *Mean flow structure*

The dramatic change to the mean wake due to a moving stud is shown in figure 8, with isocontours indicating the mean Reynolds shear stress $\overline{u'v'}/U_\infty^2$, measured with PIV in a single streamwise/radial plane. The top left image corresponds to the smooth sphere base flow. This flow pattern is essentially Re independent for higher subcritical Re (Norman & McKeon 2011*a*). With the stud moving at $\omega^* = 0.15$ (which corresponds to 1 Hz at this Re), there is very little change imparted to the wake structure. As the speed is increased, the mean separation point moves further downstream and the

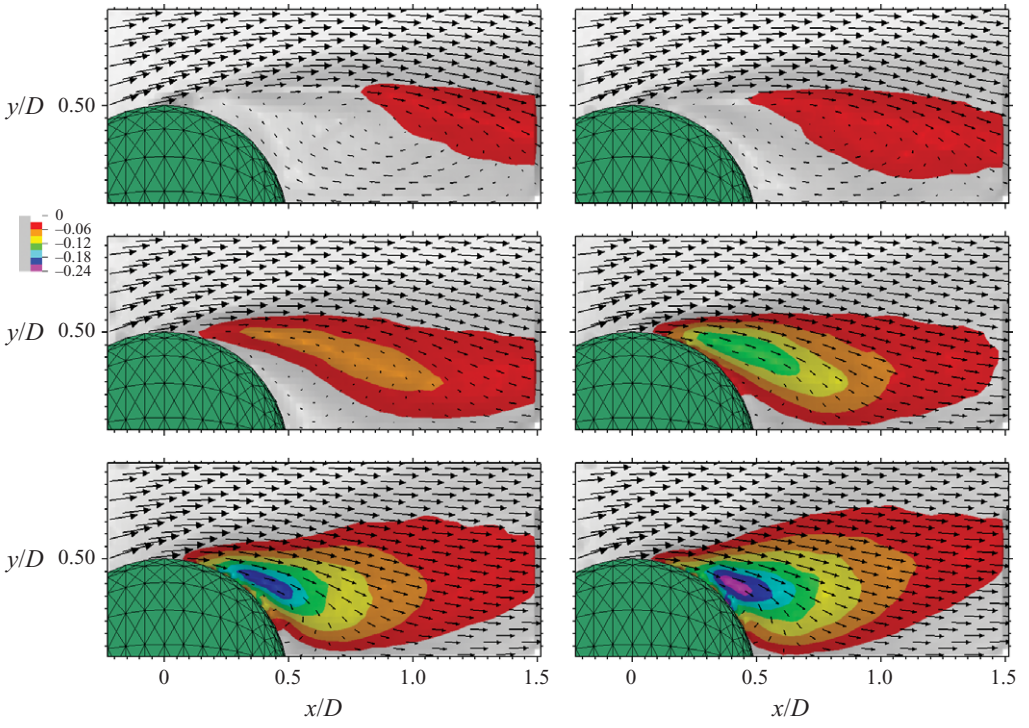

FIGURE 8. (Colour online) Mean velocity field and mean Reynolds shear stress for (left to right, then top to bottom): no stud, $\omega^* = 0.15$, 0.34, 0.52, 0.70 and 0.89.

mean wake gradually shrinks. At $\omega^* = 0.89$, the mean velocity field looks more similar to the supercritical wake than the subcritical wake (Norman & McKeon 2011*a*), though the Reynolds stresses have dramatically changed, with the maximum value being more than a factor of four larger than the supercritical case. As the stud speed is increased, the position of the maximum Reynolds shear stress also moves closer to the sphere. This is also true for the streamwise and radial Reynolds stresses (not shown).

3.4. *Instantaneous velocity fields*

An understanding of what causes the significant changes to the flow can be found by examining instantaneous velocity fields. Synchronous force and PIV measurements were taken in the top half of the x-y plane (i.e. the streamwise plane with $\theta = 0°$) for five different stud speeds, three of which are shown in figures 9–11. Image pairs were acquired at a frequency which allowed at least 100 vector fields to be calculated per stud revolution. Results for the smooth sphere, which reveal a large and slowly varying wake, can be found in Norman & McKeon (2011 *b*).

For the lower speed run ($\omega^* = 0.15$, figure 9), there is a clear effect of the stud in the force history, and the force can be related to a change in the flow field. Four velocity fields which cover one full rotation of the stud are plotted, with the first one corresponding to the time when C_y was close to a maximum, with the stud at $\theta_k = 81°$. This first velocity field has a small recirculation region, compared with the other three fields, indicating enhanced entrainment in the shear layer. This pattern repeats itself with each oscillation of the stud, with random force variations superimposed on top

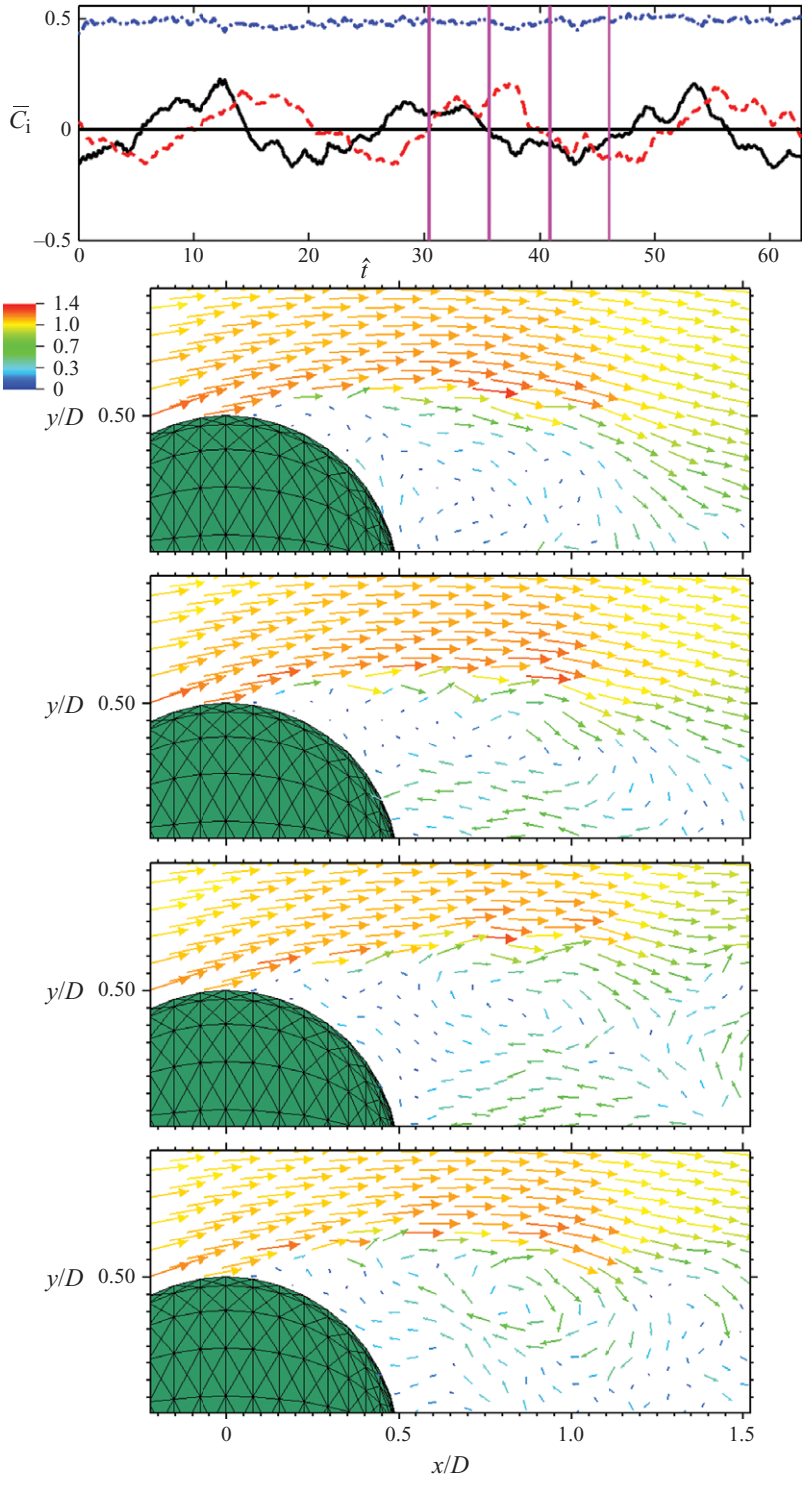

FIGURE 9. Time trace of the forces along with four instantaneous velocity fields equally spaced over one stud revolution (indicated by the vertical line on force history), with the stud moving at $\omega^* = 0.15$. The vector field is in the x-y plane, and the forces are marked as C_x (-·-); C_y (–) and C_z (- -).

of the stud frequency, as can be seen by examining the adjacent maxima on the force plot. The overriding impact of the stud allows for a phase-averaged force and flow field to be calculated, which will be described in the next section.

At a higher stud speed of $\omega^* = 0.52$, the magnitude of the lateral force becomes as large as the drag, and the wake structure is strongly modified (figure 10). Once again, when the lateral force in the PIV plane is a maximum (with the stud at $\theta_k = 123^\circ$), the flow remains attached much further downstream, and there is a very small recirculation region. The second and fourth vector fields are quite distinct, yet the mean in-plane lateral force is near zero on both, showing that there is a clear asymmetry in the wake. This also highlights the difficulty of correlating the two-dimensional velocity fields with the forces for the smooth sphere case, which experiences small-scale random forcing: the streamwise cut of the vector field is not only dependent on the in-plane force but also the out-of-plane force. Even so, the general trend for the smooth sphere case is the same, with a smaller wake when the in-plane force is large (Norman & McKeon 2011*b*).

When the angular frequency of the stud is increased to $\omega^* = 0.89$ (figure 11), the lateral forces decrease, but at the same time the mean Reynolds stresses are increased (as was observed in figure 8). At this speed the local recirculation region is essentially gone when the in-plane force reaches a maximum. This is not to say that the flow does not separate; with the wide field of view this cannot be precisely determined. Another feature is that the stud is almost on the opposite side of the sphere ($\theta_k = 162^\circ$) when the in-plane force is a maximum. The characteristics of C_D are essentially independent of ω^*.

The instantaneous velocity fields suggest the physical mechanism which is responsible for both the variation in the lateral force (figure 6) and the hot-film results (figure 7*a*). Examining a full-time series (not shown), it was found that the hot-film reading was highly correlated with the local position of separation. This holds for all of the stud speeds examined, with small variations in the predicted and actual azimuthal angle of the separation, indicating that three-dimensional effects in the wake do not need to be taken into account when interpreting the hot-film data. As an example, consider the $\omega^* = 0.15$ hot-film result in figure 7(*a*), which could be interpreted in the following manner: immediately after the stud passes, the separation point begins to move downstream, reaching a maximum streamwise angle when the hot-film voltage is a minimum, and then very gradually returning to the initial separation angle. Note that the separation angle is not directly measured, though the trends in the PIV data are clear.

The variation in the magnitude of the mean lateral force (in the stud reference frame, figure 6) has an analogous interpretation to that of the hot-film results. At low speeds, the wake is only slightly altered by the passing stud. As the speed is increased, the minimum size of the wake continues to decrease, and at the same time the azimuthal extent of delayed separation is increased. When the maximum lateral force is produced, there is a local region where there is no detectable wake in the plane of the PIV. As the speed is increased further, the azimuthal extent continues to increase, but at the same time the wake on the opposite side of the sphere begins to decrease in size due to increased fluid entrainment (as is evident in figure 7(*a*) or from the progression of the velocity fields, which are not shown); thus partially cancelling the effect on the net lateral force.

Although a planar cut of the velocity field yields significant insight into the force history, it will be shown in the next section that the position of the separation is inextricably linked to the vortical structure in the wake.

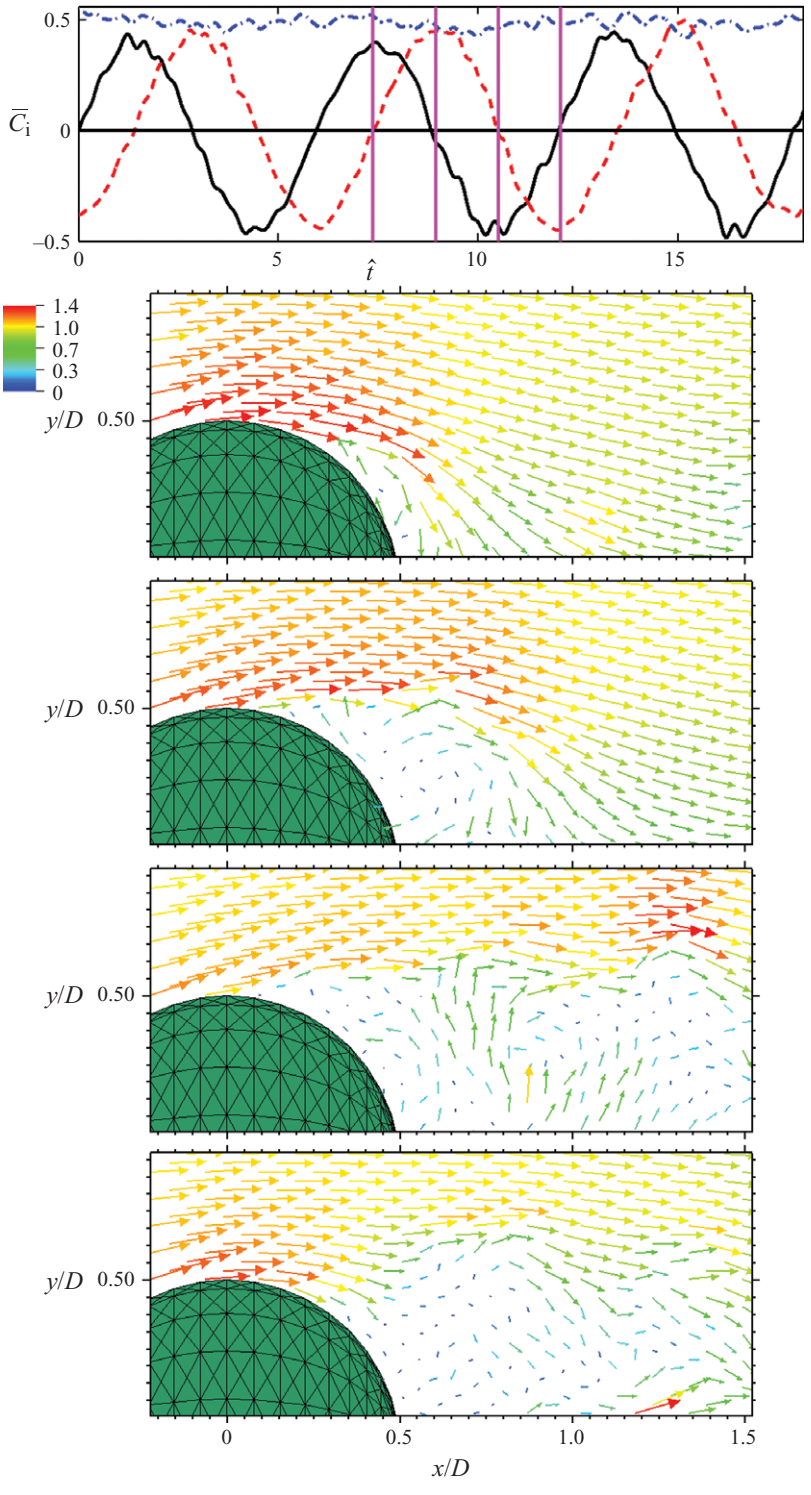

FIGURE 10. Same as figure 9, except with $\omega^* = 0.52$.

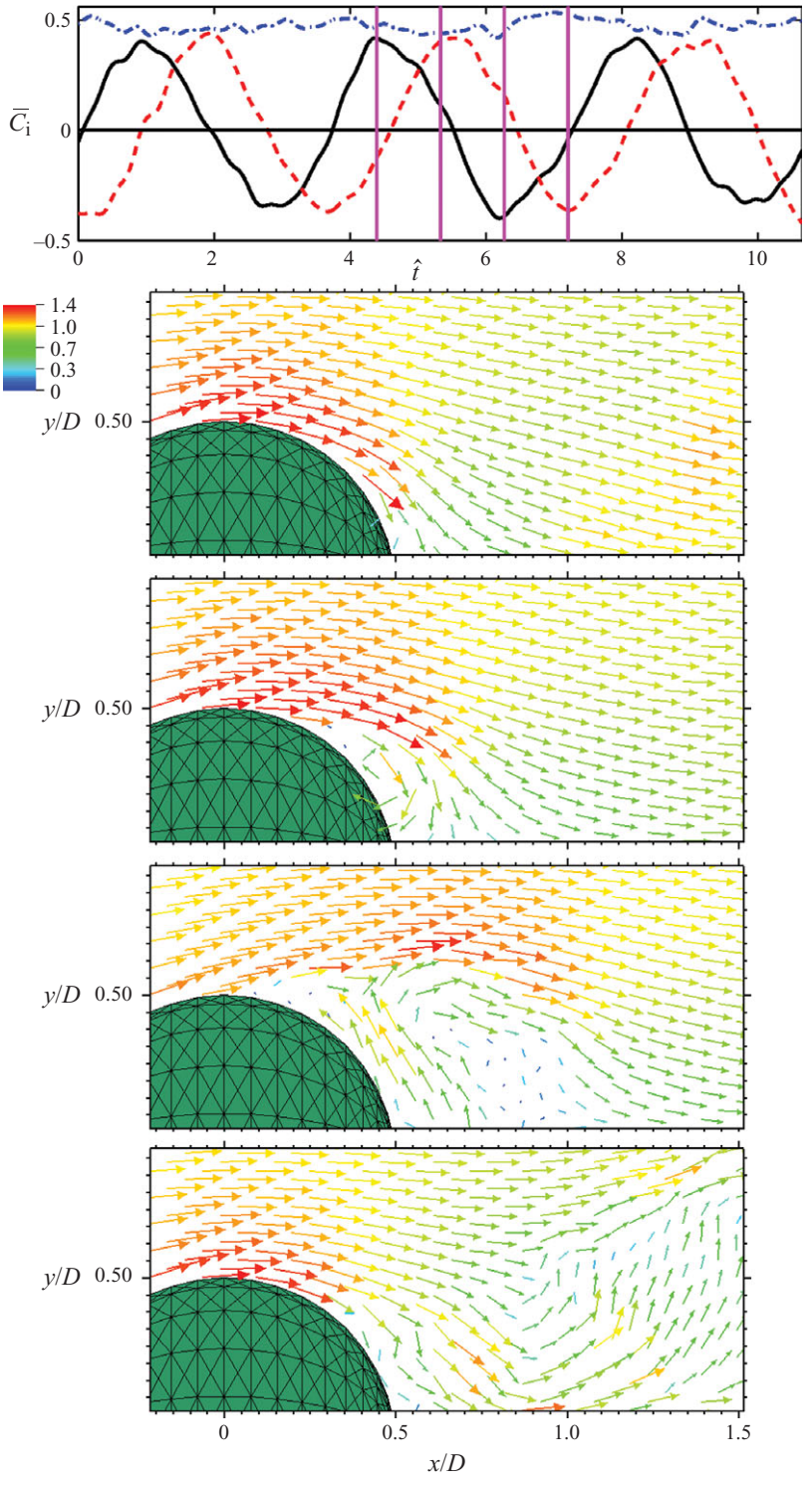

FIGURE 11. Same as figure 9, except with $\omega^* = 0.89$.

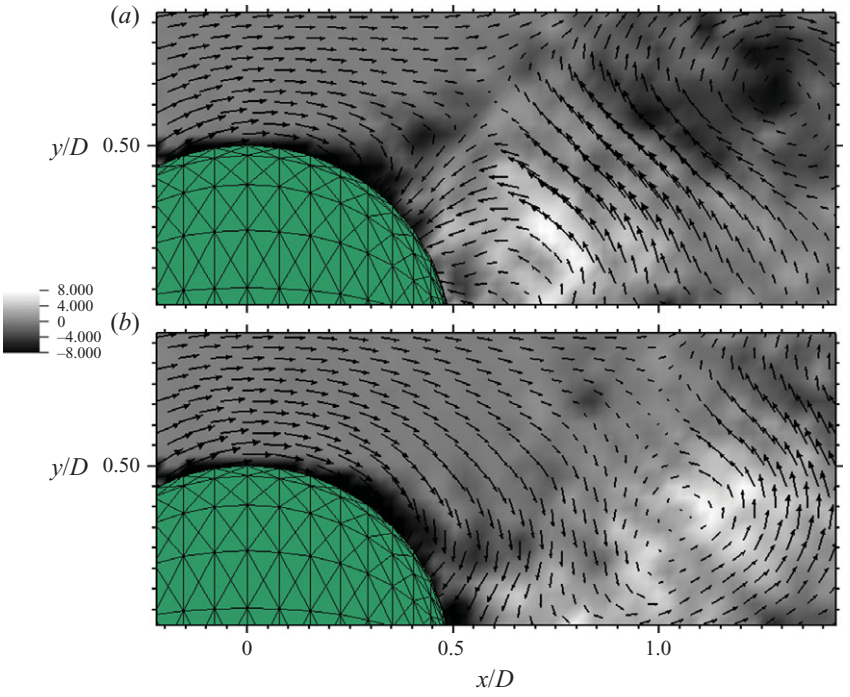

FIGURE 12. (Colour online) Phase-averaged velocity fields with $0.6U_\infty$ subtracted and with the stud moving at $\omega^* = 0.89$. Greyscale shading indicates the value of the dimensionless vorticity. (*a*) The stud is at 65° in the top image and shows a vortex that has a negative azimuthal component on the top right and a vortex that has a positive azimuthal component forming behind the sphere. (*b*) In the bottom image, the stud is at 100° and the vortex with positive azimuthal vorticity is now fully formed.

3.5. *Phase-averaged flow field*

Since the structure of the flow field is dominated by the position of the moving stud, it is possible to find a phase-averaged flow field. The azimuthal angle was divided into 100 bins, and each velocity field was placed in one of the bins based on the simultaneous measurement of the stud position. In order to average over the random variations in the wake that were not associated with the stud, time resolved PIV images were acquired for at least 12 stud revolutions per stud speed. Averaging over the velocity fields in each bin yielded 100 velocity fields, each corresponding to a different azimuthal distance from the stud.

Figure 12 shows two of these phase-averaged plots for the faster $\omega^* = 0.89$ run, $\hat{t} = 1$ and 1.6 after the stud has passed, with the separation point just beginning to move downstream. To highlight the structure in the wake, $0.6U_\infty$ was subtracted from the streamwise velocity, and the vorticity that is normal to the plane of the image is indicated using greyscale shading. This shows a pair of very clear counter-rotating vortices and hints at some very rich structure in the wake. In terms of the radial velocity, U_r (where r is in the lateral force plane and is the distance from the sting), a large positive U_r is induced between the two vortices, with negative U_r on either side. This radial velocity will be used to help interpret the structure in the wake.

To gain a better understanding of the wake structure, the phase-averaged three-dimensional wake was reconstructed out of the U_r and U_x velocity components (U_θ is not available from the planar data). This was possible because the sphere is symmetric,

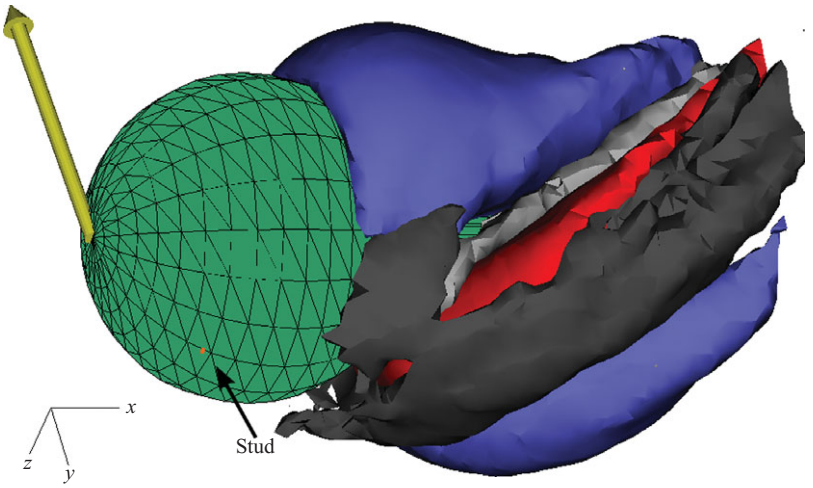

FIGURE 13. Three-dimensional phase-averaged flow field, with roughness element moving at $\omega^* = 0.89$. Normalized azimuthal vorticity contours are -3 (dark grey) and $+3$ (light grey). Normalized radial velocity contours are -0.2 (blue) and $+0.4$ (red). The lateral force vector is indicated by the arrow at the front of the sphere.

with the only important variable being the position of the PIV plane (always at $\theta = 0°$) compared with the position of the stud. Thus, when the phase-averaged stud position is located at 20°, the phase-averaged velocity field is $-20°$ from the stud. In this way the three-dimensional phase-averaged wake was constructed, with the stud chosen to be at $\theta = 0°$.

Figure 13 shows both contours of radial velocity (in red and blue) and azimuthal vorticity (greyscale) for the fast $\omega^* = 0.89$ case, where the velocity and vorticity have been normalized using the free stream velocity and sphere diameter. The vorticity contours lie in between the positive and negative velocity contours, indicating that the radial velocity provides a reasonable indication as to the location and shape of the counter-rotating vortices. The azimuthal vorticity does not provide a good indication of the structure in the wake at lower stud speeds because the vorticity is then mostly aligned with the streamwise direction. Thus, the radial velocity will be used to highlight the structure in the wake as a function of stud speed.

Figures 14–18 show contours of the phase-averaged radial velocity for several different stud speeds. Both a front- and a back-angled view are shown, with the approximate position of the stud indicated. The orientation and contour levels are the same for all plots and were chosen in an attempt to highlight the vortical structure. In addition, the lateral force vector (which corresponds to the phase-averaged force when the stud is at $\theta = 0°$) is shown on the front of the sphere and has the same scale between figures.

The phase-averaged wake for the lowest speed (figure 14) is mostly symmetric, with a small change in the wake due to the passing of the stud (which is moving clockwise as viewed from upstream) indicated by the streak of negative U_r and also by the decrease of positive U_r near the equator, both due to a local change in the position of separation and the size of the wake.

When the angular frequency is increased to $\omega^* = 0.34$ (figure 15), the extent of the affected area is increased, and from the downstream view some of the fluid has a

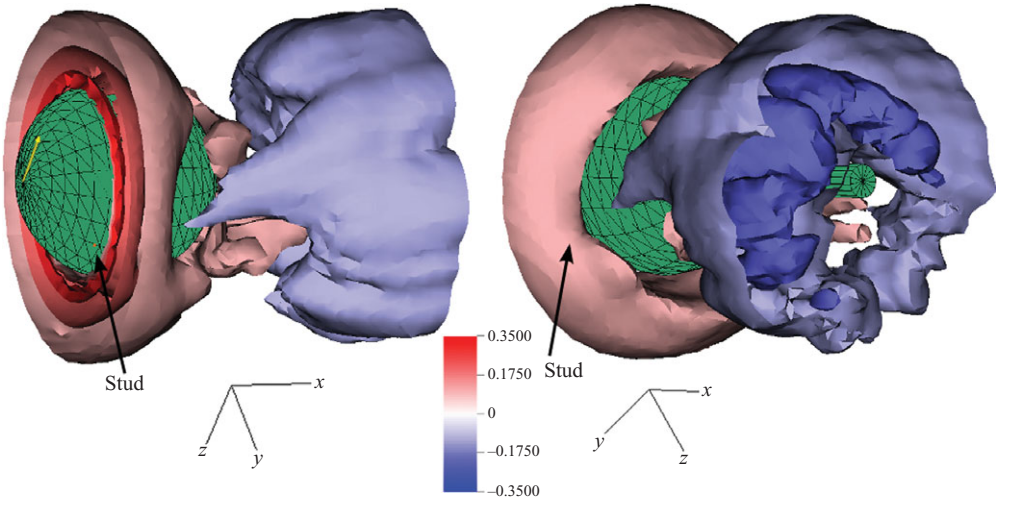

FIGURE 14. (Colour online) Angled views showing the radial component of the phase-averaged wake, with $\omega^* = 0.15$. Contours are of normalized radial velocity: −0.2, −0.1, 0.1, 0.2, 0.3 and 0.4.

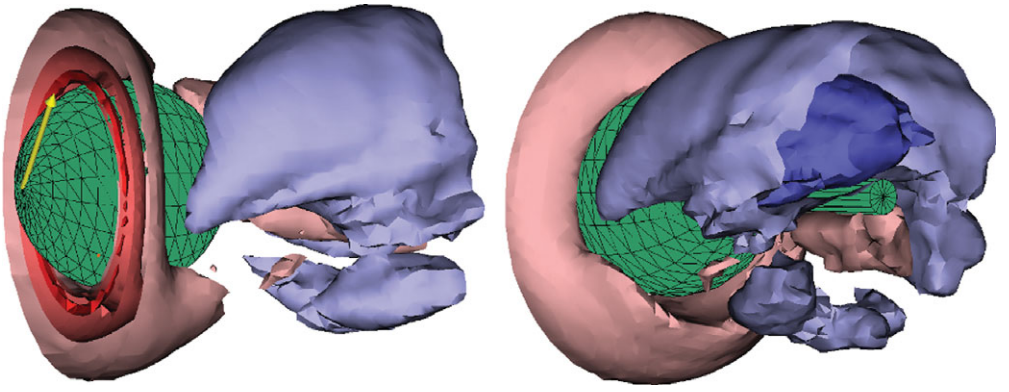

FIGURE 15. (Colour online) Same as in figure 14, with $\omega^* = 0.34$.

negative velocity greater than $0.2U_\infty$ near the sting, indicating that the fluid passes from the upper to the lower plane, with the sign of its velocity changing.

In figures 16–18 the stud frequency is greater than $\omega^* = 0.5$, and there is a clear signature of the pair of counter-rotating vortices following a helical path. As the stud moves faster, the streamwise wavelength of the helices gets shorter. In all cases the orientation of the structure in the wake is well correlated with the position of the stud.

The orientation of this helical vortex pair is such that it induces a velocity field (due to the azimuthal vorticity) that would contribute to locally keeping the sphere boundary layer attached further downstream. For comparison, the effect of a trip wire in the subcritical regime is to keep the flow attached until about 120°, thereby leaving a recirculating region behind the sphere (Bakić 2004). Thus, it is possible that tripping the boundary layer alone would keep the flow attached to about 120°, while the addition of the large-scale vortices in the wake appears to locally suppress separation (as in figure 11).

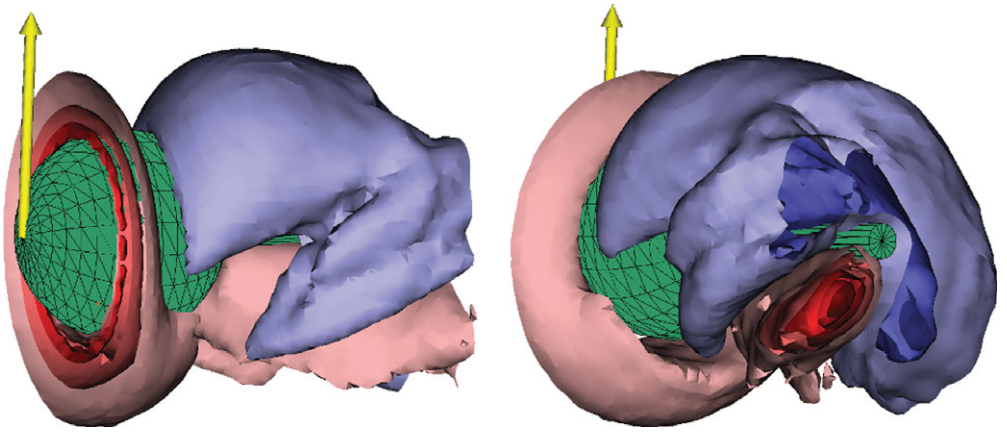

FIGURE 16. (Colour online) Same as in figure 14, with $\omega^* = 0.52$.

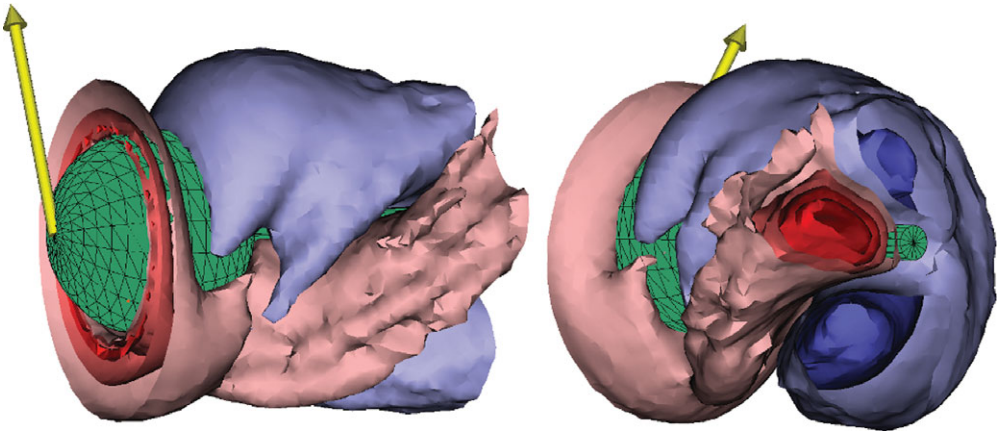

FIGURE 17. (Colour online) Same as in figure 14, with $\omega^* = 0.70$. Note the high speed positive velocity fluid, with negative U_r fluid on either side, indicating counter-rotating vortices in the shape of a helix.

For a static stud, it was argued (Norman & McKeon 2011*a*) that increased entrainment locally causes the flow to stay attached slightly further downstream than for the rest of the flow, producing weak counter-rotating vortices through the roll-up of the separating shear layer with mutual induction towards the sting (figure 19). Here, this idea is extended to the case of a dynamic stud and illustrated with a simple schematic of a spanwise cut of the near wake, ignoring three-dimensionality (figure 20). The dashed circle represents the centre of the mean shear layer for the base flow, and the arrows represent the change in the shear layer caused by the stud with each view oriented such that the force is in the $+y$-direction. Figure 20(*a*) represents a spanwise cut of figure 19. As the stud begins to move at low speeds (figure 20*b*), an extended region of the flow is tripped, causing the flow to remain attached over a larger portion of the sphere, with the inward moving fluid being forced towards the un-tripped region, again producing two counter-rotating vortices that are stronger and further apart. Finally, when the stud is moving fast as compared to the time scale associated with the movement of the separation location (figure 20*c*), most of the flow remains attached to the sphere, causing the fast moving fluid to be

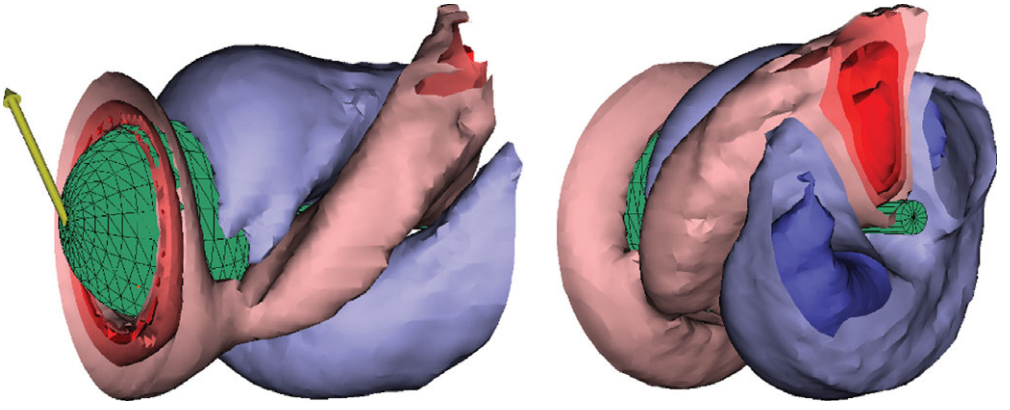

FIGURE 18. (Colour online) Same as in figure 14, with $\omega^* = 0.89$.

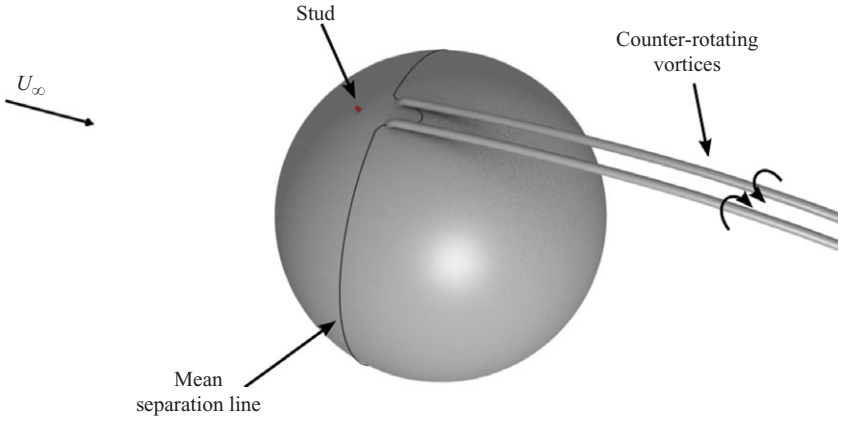

FIGURE 19. (Colour online) The stationary stud locally delays separation in the subcritical regime, likely leading to the production of weak counter-rotating vortices.

forced towards the only region that has not been tripped and producing two very strong counter-rotating vortices with mutual induction away from the centre (similar to supercritical flow with a static stud), as opposed to towards the centre. This of course is a very simplified explanation because the flow not only moves out of the plane, but the time-dependence of the disturbance also produces the helical shape, which influences the dynamics of the separation.

3.6. *Implications for flow over a smooth sphere*

The sensitivity of the boundary layer and separated shear layer to small surface perturbations yields significant insight into the base flow. The long time scale associated with the movement of the separation point is likely to be still present for the smooth sphere due to amplification of free stream perturbations. As the local separation point is delayed, a small side force is exerted on the sphere, and very weak counter-rotating vortices are also likely to be formed, as was also suggested for the case of an isolated roughness element. The superposition of many perturbations along the azimuthal direction would lead to a separation line that slightly varies about the mean in both a temporal and spatial sense. This provides one explanation for the cause of the very low frequency forcing on a sphere that was observed for subcritical Reynolds numbers in the numerical studies of Constantinescu & Squires

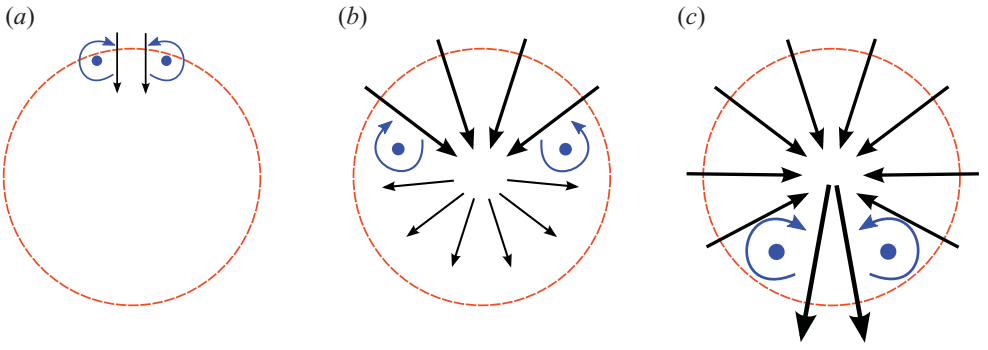

FIGURE 20. (Colour online) Schematic simplification of a spanwise cut of the near wake, showing the progression of the counter-rotating vortices as the region of influence of the stud increases: (*a*) the static stud produces vortices which push each other towards the centre, (*b*) vortices move away from each other and (*c*) meet on the opposite side, now pushing each other away from the centre.

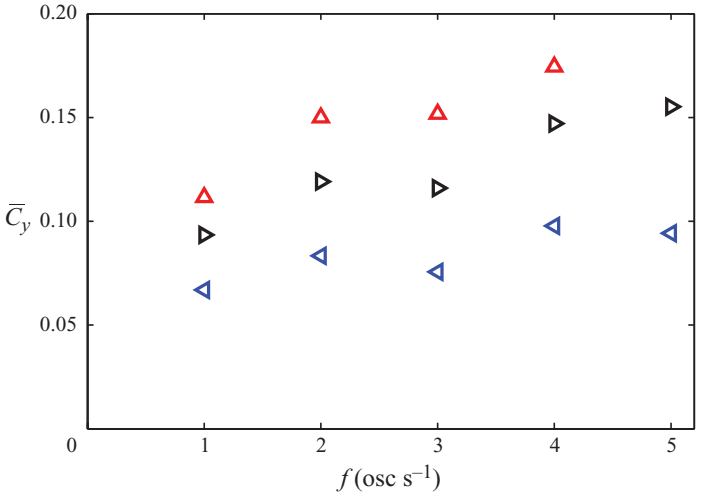

FIGURE 21. (Colour online) Mean lateral force ($\overline{C}_y$), with stud oscillating about $\theta = 0°$ and amplitude: $\pm 40°$ (◁); $\pm 60°$ (▷); and $\pm 80°$ (△). $\overline{C}_x$ and $\overline{C}_z$ were not notably changed.

(2004) and Yun, Kim & Choi (2006) and later experimentally verified and extended by Norman & McKeon (2011*b*). An additional (likely to be intrinsically linked) explanation rests with the meandering of large-scale three-dimensional structures in the wake.

4. Results: shaped stud trajectories

In order to gain further insight into the flow, the following sections briefly examine the effect of an oscillating stud, the effect of shaping the stud trajectory and the step response of the flow to a change in the stud's angular frequency.

4.1. *Oscillating roughness element*

To demonstrate that it is possible to produce a mean lateral force, the stud was oscillated about the y-axis ($\theta = 0°$) with varying frequency and amplitude (figure 21).

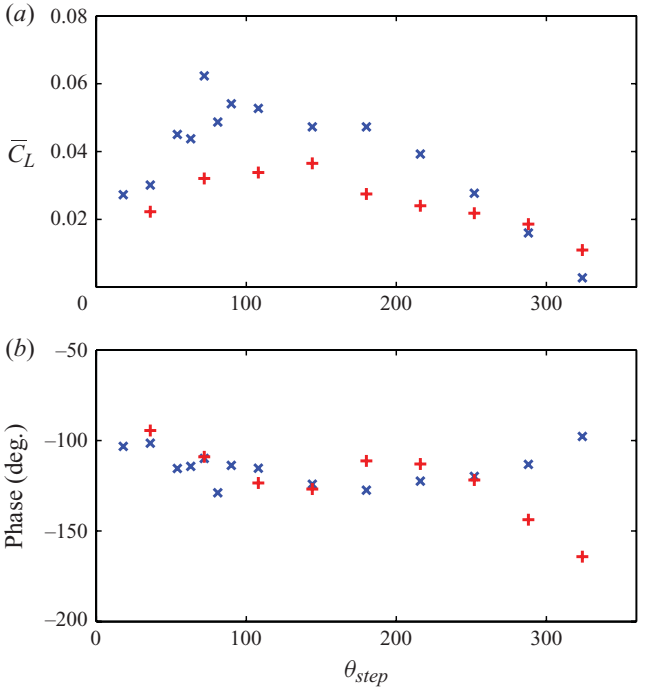

FIGURE 22. (Colour online) (*a*) Mean lateral force, and (*b*) phase for shaped trajectories, with a step up in angular frequency at θ_{step} and a step back down at $\theta = 0°$: $\omega^* = 0.17$–$0.55(\times)$; 0.34–$0.55(+)$.

The stud motion consisted of a rapid ramp to constant speed terminated by rapid deceleration, i.e. the stud displacement was not sinusoidal. The general trend is that as the frequency or amplitude of the oscillations increase, so does the mean side force, providing more evidence that the stud locally alters the separation point. The low amplitude, low speed oscillations of the stud produced a mean side force of about 1.8 times larger than that produced by a static stud, whereas the high amplitude, high speed mean oscillations caused a side force that was about 4.6 times larger. However, when a trip-wire was placed over half of the sphere a mean side force of $C_y = 0.38$ was produced, which indicates that there is still a large margin for increasing the mean side force, especially considering that our approach produces structure in the wake which could be shaped to produce an even greater side force.

4.2. *Velocity profile shaping*

Figure 22 shows the effect of shaping the trajectory of the stud such that ω^* depends only on θ, with the intent of producing a mean side force without changing the direction of rotation. For the constant frequency case, a fast moving stud produces a large instantaneous lateral force, while a slow-moving stud produces a small lateral force. This indicates that it should be possible to obtain a mean lateral force with the stud moving in just one direction, by varying its speed. To verify this, the stud frequency was set to a constant small value ($\omega^* = 0.17$ or 0.34) at $\theta = 0°$, then at θ_{step} it was increased to $\omega^* = 0.55$ (figure 22). The step response of the motor was not instantaneous, so the LQR preview controller was used to smooth out the step and produce an optimal transition without overshoot. The mean lateral force and phase are plotted, where the phase is defined here to be the angle between the centre of the low frequency region ($\theta_{step}/2$) and the mean lateral force vector.

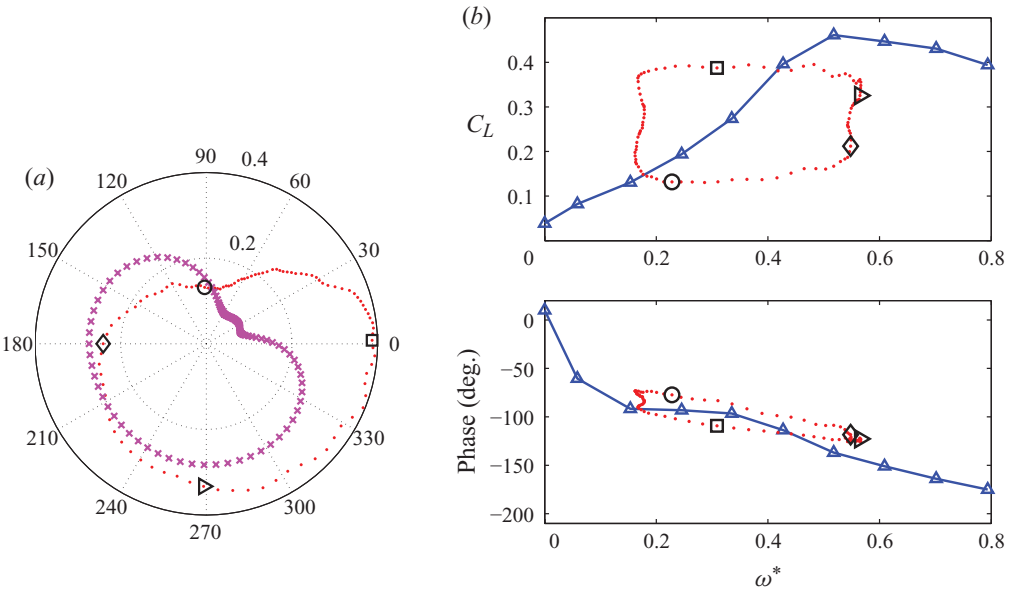

FIGURE 23. (Colour online) Shaped trajectory corresponding to a step from $\omega^* = 0.17$ to 0.55 at 90°. (*a*) The angular coordinate is the stud position with the stud moving counter-clockwise: phase-averaged force (...); $\omega^*/2$ (x). (*b*) Mean C_L and phase $(\theta - \theta_k)$ vs. constant frequency ω^* results for $Re = 0.5 \times 10^5$ (△), compared with the current trajectory.

The largest mean lateral force occurs approximately when the stud is moving slowly for a 90° span and rapidly for the rest of the revolution. When it is moving slowly, the local separation point is not significantly changed. However, if too much time is spent moving slowly on one side, the delayed separation begins to move back upstream on the other side of the sphere. The magnitude of the mean lateral force is similar to that of the oscillating stud that has a frequency of 1 Hz and covers a span of ±40°. This is not very large, but the non-constant angular frequency gives insight into the dynamics. Note that the significant scatter in the data is due to the forces being very small ($C_L = 0.01$ corresponds to 3 mN). This has a big effect on estimating the angle to the mean force when the force is small.

The angle to the mean force generally points to about −120° away from the centre of the low frequency region (figure 22*b*). This clearly points to an effect of three-dimensionality, as the direction of rotation is important.

One example of a shaped trajectory is shown in figure 23(*a*), corresponding to a step from $\omega^* = 0.17$ to 0.55 at 90° and a step back down at 360°/0°. Both the phase-averaged force and the angular frequency (scaled by a factor of two) are plotted against the position of the stud, demonstrating precise control of the stud trajectory and a difference in the orientation of the force trajectory and the stud frequency, due in part to the time delay associated with the movement of the separation location.

The lateral force and phase as a function of stud speed are compared with the constant frequency results in figure 23(*b*). The range of the phase for the constant frequency case, between $\omega^* = 0.17$ and 0.55, is not very large and neither is the range for the shaped trajectory. On the other hand, the lateral force for the constant frequency case changes significantly and so does that of the shaped trajectory. The large open symbols are the same in figures 23(*a*) and 23(*b*) and show the direction of the hysteresis. Starting at the bottom left of the rectangle (adjacent to the open

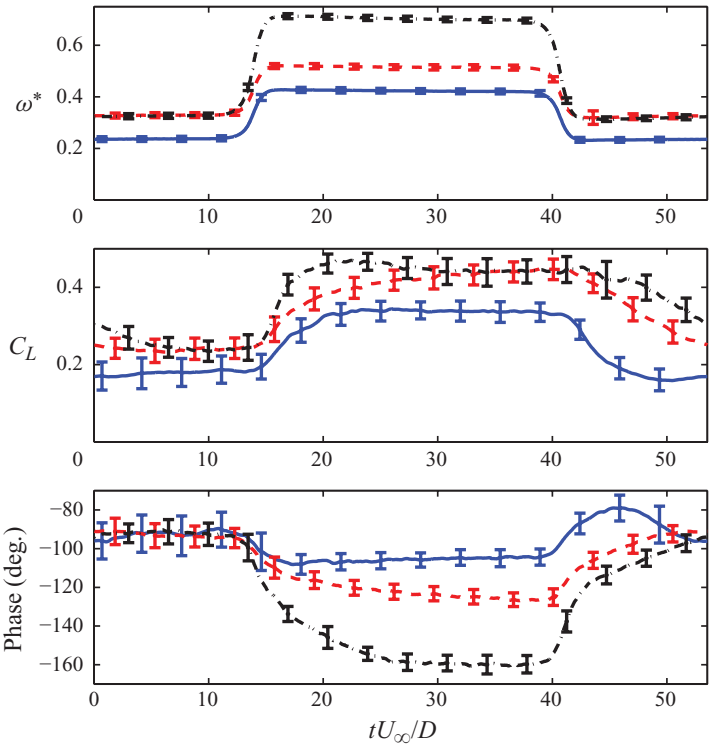

FIGURE 24. (Colour online) Three mean step responses, each averaged over 120 periods, with the error bars indicating $\pm\sigma$. The phase is defined to be the angle between the $\theta_{step}/2$ and the mean lateral force vector.

circle in figure 23*b*): the force is small when the stud speed increases quickly. When the stud has reached the higher speed, the force gradually increases. Note that there is a small variation in the nominally constant angular frequency. While the stud slows down, there is little change to the force, and then at low speed the lateral force gradually decreases again. This is explained by the dynamics of the attachment region: the stud produces a local disturbance that excites the instabilities in the flow, which gradually locally change the location of separation. It is this time delay which causes the hysteresis.

4.3. *Effect of a step change in angular frequency*

Figure 24 shows a preliminary investigation of the time response of the system due to a step change in the actuation frequency. Here, the motor 'step' in frequency takes about $\hat{t} = 3$, where the frequency step is a function of time, as opposed to θ as in the previous section. This is slightly faster than the $\hat{t} \approx 4$ for the separation point to locally move to its furthest downstream position after the stud passes. The results are an average over 120 periods, with the error bars indicating the standard deviation $\pm\sigma$. The variation of the motor speed from one period to the next is very small, while that of the lateral force and phase are large. This standard deviation of the forces is close to that for the no stud case ($\sigma = 0.5$, see Norman & McKeon 2011*b*), indicating that they are of similar origin, with the random fluctuations of the wake superimposed on top of the effect due to the stud. Thus, for control purposes, it is

not possible to say what force a certain stud trajectory will produce, but only what force it will produce on average.

This plot indicates some of the interesting dynamics that could be exploited with a control scheme. For example, the response time of the wake to an increase in frequency is much faster than the response time to a decrease, for all the three steps. This is explained by the hot-film results (figure 7) for the lowest stud speed, which showed a peak response to the passing of the stud after $\hat{t} \approx 4$, while the decay back to the base flow took $\hat{t} \approx 30$. Another interesting feature is the overshoot of the phase lag for the smallest step down and also the slow change in the phase for the largest step up. This rich behaviour not only opens up a lot of possibilities for a control scheme but also makes the problem very challenging.

5. Conclusions

The effect of a time-dependent perturbation to the surface of a sphere was examined by varying the position of a local roughness element (a stud) in real time. It was found that this produced a significant change in the flow field, much larger than that caused by a static stud. This was linked to the long time scale associated with the dynamics of a changing separation line. Hot-film and particle image velocimetry results revealed that after the stud passed by the streamwise measurement plane, the local position of flow separation gradually moved downstream, reaching a maximum downstream position after about $\hat{t} = 4$, and then slowly returning back to the initial position of separation. This time scale was nearly independent of the stud speed, and the effect was attributed to an excitement of the boundary and shear layer instabilities, which increases fluid entrainment and keeps the flow attached, with the azimuthal extent at any given time being dependent on the speed of the stud.

It was found that an instantaneous lateral force as large as the drag was produced when the dimensionless angular stud frequency was $\omega^* \approx 0.5$. This is close to a subharmonic of the wake instability, which Chomaz *et al.* (2006) referred to as the helical instability. PIV and hot-film revealed that this maximum force was produced when the flow separated near the back of the sphere in the streamwise plane associated with the force direction (the first side) and near the equator on the opposite side (the second side). At lower stud speeds, the flow did not remain attached as far downstream on the first side, yet it still separated near the equator on the second side, leading to a smaller net force. At higher speeds, the local separation point cannot move any further downstream on the first side, and on the second side the separation near the equator begins to move downstream, cancelling the net effect on the lateral force magnitude.

The time-dependence of the stud position leads to the production of a coherent structure in the wake, the details of which are dependent on the stud speed. A planar PIV velocity field in the streamwise/radial plane revealed two counter-rotating vortices with a mutual induction that moved them away from the sting in the subcritical case. Because the flow field is strongly dependent on the stud motion, it was possible to construct a phase-averaged velocity field based on the angle between the stud and the PIV plane. Only two of the three velocity components were measured, but the structure of the wake can be visualized using just the radial velocity component. By relating the three-dimensional radial velocity contours to the counter-rotating vortices, it was determined that these vortices form a helical shape. The orientation of these vortices was such that the induced velocity field would help to locally keep the flow attached to the sphere.

The production of the counter-rotating vortices was described using a simplified two-dimensional schematic, showing that at near zero speed the vortices are formed with mutual induction towards the sting. As the extent of the boundary layer trip is increased, these vortices move away from each other and meet on the opposite side of the sphere with the mutual induction now away from the sting. This mechanism is likely to be relevant to both the smooth sphere and distributed roughness flows as well.

Finally, the forces arising from the non-constant stud trajectories were briefly explored. It was demonstrated that a mean side force could be obtained by oscillating the stud about a point in the azimuthal direction. A mean side force of almost five times that of a static stud was achieved by moving the stud between $\pm 80^\circ$ at a frequency of 4 Hz. The mean force due to a trip wire being placed over half of the sphere was almost twice as large, indicating that a larger mean side force would likely be achieved by oscillating the stud at a higher frequency. In addition, it was also shown that it is possible to develop a small mean side force by preferentially changing the speed of the stud depending on its position, without completely changing directions as with the oscillating stud.

The support of NSF-CAREER award number 0747672 (program managers W. W. Schultz and H. H. Winter) is gratefully acknowledged.

Appendix. Control of stud location

In this section, we detail the design of the LQR controller which regulated the position of the roughness element on the sphere surface. In order to calculate the LQR gains, it is convenient to put the equations in state-space form. Using standard notation (see, e.g. Åström & Murray 2008),

$$\dot{x} = Ax + Bu, \tag{A 1}$$

$$y = Cx + Du, \tag{A 2}$$

where x is the state vector, u is the control input, y is the measured output and A, B, C, and D are constant matrices. Defining $x_1 = \theta$, $x_2 = \dot{\theta}$, and $x_3 = \mathrm{i}$, with measurements $y_1 = \theta$ and $y_2 = \mathrm{i}$, combined with the governing equations yields

$$\frac{d}{\mathrm{d}t}\begin{pmatrix}\theta\\ \dot{\theta}\\ \mathrm{i}\end{pmatrix} = \begin{pmatrix}0 & 1 & 0\\ 0 & -b/J & K_t/J\\ 0 & -K_t/L & -R/L\end{pmatrix}\begin{pmatrix}\theta\\ \dot{\theta}\\ \mathrm{i}\end{pmatrix} + \begin{pmatrix}0\\ 0\\ 1/L\end{pmatrix}V, \tag{A 3}$$

$$y = \begin{pmatrix}y_1\\ y_2\end{pmatrix} = \begin{pmatrix}1 & 0 & 0\\ 0 & 0 & 1\end{pmatrix}\begin{pmatrix}\theta\\ \dot{\theta}\\ \mathrm{i}\end{pmatrix}. \tag{A 4}$$

With the voltage as the control input, precise control of θ could only be accomplished if there was no uncertainty in the system. Since this is impossible, feedback was added in order to control the position of the roughness element. Defining the control input to be dependent on the state of the system and the setpoint, $u = Kx + Mr$ gives

$$\dot{x} = A_K x + B_K r, \tag{A 5}$$

$$y = C_K x + D_K r, \tag{A 6}$$

where $A_K = A + BK$, $B_K = BM$, $C_K = C + DK$ and $D_K = DM$. The feedforward gain M was found by setting $\dot{x} = 0$ and noting that θ should equal r in steady state. The feedback gain K was found by minimizing the cost function,

$$J \equiv \int_0^\infty [x(t)^{\mathrm{T}} Q x(t) + u(t)^{\mathrm{T}} R u(t)]\,\mathrm{d}t = \int_0^\infty [x(t)^{\mathrm{T}} Q x(t) + u(t)^2]\,\mathrm{d}t, \tag{A 7}$$

subject to (A 1) and $u(t) = Kx(t)$. There is only one input, and hence R can be set to 1 without loss of generality since the solution is a function only of the ratios of the components of Q to R.

In order to avoid sharp high-amplitude changes in the voltage when there are step changes in the angular frequency and instead have an optimal transition, a preview controller was also implemented. Instead of simply supplying the desired position or velocity, a few hundred milliseconds of the future setpoints was also passed to the controller. This is more easily explained by considering the following suitably defined discrete-time model, where the input is applied with a zero-order hold:

$$\tilde{x}_{j+1} = A_p \tilde{x}_j + B_p u_j, \tag{A 8}$$

$$y_{j+1} = C_p x_j + D_p u_j. \tag{A 9}$$

Now, the state is augmented to include the future N setpoints ($r_{\mathrm{i}} = \theta_{set}(t + j\Delta t)$, $j = 0, \ldots, N$ and Δt is the sample period):

$$\tilde{x} \equiv \begin{pmatrix} \theta \\ \dot{\theta} \\ \mathrm{i} \\ r_0 \\ r_1 \\ \cdot \\ \cdot \\ r_N \end{pmatrix}. \tag{A 10}$$

The equivalent discrete-time system's dynamics matrix $\Phi := \mathrm{e}^{A\Delta t}$ is augmented with an $(N+1) \times (N+1)$ matrix, which shifts the setpoint values up by one time step:

$$A_p \equiv \begin{pmatrix} \Phi & 0 \\ 0 & A_r \end{pmatrix}, \tag{A 11}$$

where A_r is the following matrix of compatible dimensions:

$$A_r \equiv \begin{pmatrix} 0 & I_N \\ 0 & 0 \end{pmatrix}. \tag{A 12}$$

Here, u is still the applied voltage, and B_p was obtained by augmenting the discrete-time control matrix by a zero column vector of length $N + 1$. The C and D matrices were padded with zeros to reach the appropriate size since no new states were being measured. The control input (the voltage) was set to be dependent on all of the augmented states: $u_j = K_p \tilde{x}_j$. Note that a feedforward matrix M is not needed if the preview horizon N is sufficiently large.

With the new state space that includes a preview of the upcoming trajectory/velocity, a similar routine was followed to optimize the voltage: a series of gains were found

by minimizing the following discrete-time cost:

$$J_p \equiv \sum_{j=0}^{\infty} \tilde{x}_j^T Q_p \tilde{x}_j + u_j^2. \tag{A 13}$$

In order to penalize an error in position, Q_p was given by

$$Q_p = \begin{pmatrix} q & 0 & 0 & -q & & \\ 0 & 0 & 0 & 0 & & \\ 0 & 0 & 0 & 0 & & \\ -q & 0 & 0 & q & & \\ & & & & \ddots & \\ & & & & & 0 \end{pmatrix}, \tag{A 14}$$

where q is to be determined from the minimization given in (A 13). When multiplied out this just gives $x^{\mathrm{T}} Q_p x = \mathrm{e}^{\mathrm{T}} q e$, where $e := \theta - r_0$.

In order to provide reduced noise measurements to the LQR controller, a Kalman filter was implemented to provide an estimate of the state. It was designed by first augmenting the continuous-time system with a constant unknown additive disturbance d acting on $\dot{\theta}$, to take account of unmodelled effects such as the damping actually being a function of angular frequency. Defining the augmented state as

$$\bar{x} \equiv \begin{pmatrix} x \\ d \end{pmatrix}, \tag{A 15}$$

and with measured variables

$$y \equiv \begin{pmatrix} \theta \\ \mathrm{i} \end{pmatrix}, \tag{A 16}$$

the continuous-time model was converted to an equivalent discrete-time model of the form

$$\bar{x}_{j+1} = \bar{\Phi} \bar{x}_j + \bar{\Gamma} u_j + \bar{G} w_j, \tag{A 17}$$

$$y_j = \bar{C} \bar{x}_j + \bar{D} u_j + v_j, \tag{A 18}$$

where w_j represents process noise and v_j denotes measurement noise. Under the assumption that the covariance matrix of the process noise was the identity matrix, the method described by Rajamani & Rawlings (2009) was applied to some measured data in order to estimate $\hat{G}$ and the covariance matrix of the measurement noise. It was found that a $\hat{G}$ with column rank 2 gave acceptable performance when designing the Kalman filter.

REFERENCES

Achenbach, E. 1974 The effects of surface roughness and tunnel blockage on the flow past spheres. *J. Fluid Mech.* **65** (1), 113–125.

Åström, K. J. & Murray, R. M. 2008 *Feedback Systems: An Introduction for Scientists and Engineers*. Princeton University Press.

Bakić, V. 2004 Experimental investigation of a flow around a sphere. Thermal Sciences, Vol. 8, 63–81.

Bearman, P. W. & Harvey, J. K. 1976 Golf ball aerodynamics. *Aeronaut. Q.* **May**, 112–122.

Chomaz, J. M., Bonneton, P. & Hopfinger, E. J. 2006 The structure of the near wake of a sphere moving horizontally in a stratified fluid. *J. Fluid Mech.* **254**, 1–21.

Constantinescu, G. S. & Squires, K. D. 2004 Numerical investigations of flow over a sphere in the subcritical and supercritical regimes. *Phys. Fluids* **16** (5), 1449.

Darabi, A. & Wygnanski, I. 2004*a* Active management of naturally separated flow over a solid surface. Part 1. The forced reattachment process. *J. Fluid Mech.* **510**, 105–129.

Darabi, A. & Wygnanski, I. 2004*b* Active management of naturally separated flow over a solid surface. Part 2. The separation process. *J. Fluid Mech.* **510**, 131–144.

Jeon, S., Choi, J., Jeon, W., Choi, H. & Park, J. 2004 Active control of flow over a sphere for drag reduction at a subcritical Reynolds number. *J. Fluid Mech.* **517**, 113–129.

Jukes, T. N. & Choi, K. S. 2009*a* Flow control around a circular cylinder using pulsed dielectric barrier discharge surface plasma. *Phys. Fluids* **21**, 084103.

Jukes, T. N. & Choi, K. S. 2009*b* Long lasting modifications to vortex shedding using a short plasma excitation. *Phys. Rev. Lett.* **102** (25), 254501.

Kim, H. J. & Durbin, P. A. 1988 Observations of the frequencies in a sphere wake and of drag increase by acoustic excitation. *Phys. Fluids* **31**, 3260.

Norman, A. K. & McKeon, B. J. 2011*a* The effect of a small isolated roughness element on the forces on a sphere in uniform flow. (submitted).

Norman, A. K. & McKeon, B. J. 2011*b* Simultaneous force and velocity field measurements in sphere flow from subcritical to supercritical Reynolds numbers. (submitted).

Raffel, M., Willert, C., Wereley, S. & Kompenhans, J. 2007 *Particle Image Velocimetry: a Practical Guide*. Springer.

Rajamani, M. R. & Rawlings, J. B. 2009 Estimation of the disturbance structure from data using semidefinite programming and optimal weighting. *Automatica* **45** (1), 142–148.

Seifert, A., Greenblatt, D. & Wygnanski, I. J. 2004 Active separation control: an overview of Reynolds and Mach numbers effects. *Aerosp. Sci. Technol.* **8** (7), 569–582.

Taneda, S. 1978 Visual observations of the flow past a sphere at Reynolds numbers between 10^4 and 10^6. *J. Fluid Mech.* **85** (1), 187–192.

Williams, D. R., Tadmor, G., Colonius, T., Kerstens, W., Quach, V. & Buntain, S. 2009 Lift response of a stalled wing to pulsatile disturbances. *AIAA J.* **47** (12), 3031–3037.

Yun, G., Kim, D. & Choi, H. 2006 Vortical structures behind a sphere at subcritical Reynolds numbers. *Phys. Fluids* **18**, 015102.